IEEE Access
Multidisciplinary | Rapid Review | Open Access Journal

Received December 12, 2018, accepted January 27, 2019, date of publication February 6, 2019, date of current version February 27, 2019.

Digital Object Identifier 10.1109/ACCESS.2019.2897921

Hybrid Ray-Tracing/FDTD Method for Human Exposure Evaluation of a Massive MIMO Technology in an Industrial Indoor Environment

SERGEI SHIKHANTSOV[1], ARNO THIELENS[1,2], GÜNTER VERMEEREN[1], (Member, IEEE), EMMERIC TANGHE[1], PIET DEMEESTER[1], (Fellow, IEEE), LUC MARTENS[1], (Member, IEEE), GUY TORFS[1], (Member, IEEE), AND WOUT JOSEPH[1], (Senior Member, IEEE)

[1]Department of Information Technology, Ghent University–imec, 9052 Ghent, Belgium
[2]Berkeley Wireless Research Center, Department of Electrical Engineering and Computer Sciences, University of California at Berkeley, Berkeley, CA 94704, USA

Corresponding author: Sergei Shikhantsov (sergei.shikhantsov@ugent.be)

This work was supported by the Excellence of Science (EOS) Project Multi-Service Wireless Network MUlti-SErvice Wireless NETworks (MUSE-WINET). The work of A. Thielens was supported by the Research Foundation - Flanders (FWO) [PEGASUS][2]. The work of P. Demeester was supported by the European Research Council (ERC) through ATTO: A new concept for ultra-high capacity wireless networks under Grant 695495.

ABSTRACT This paper presents a numerical approach for massive multiple-input multiple-output (MIMO) human exposure assessment. It combines ray-tracing for the estimation of the wireless channel and the finite-difference time-domain method to simulate the exposure of a realistic human phantom. We apply it to estimate the exposure in a model of an industrial indoor environment with a single massive MIMO base station (BS). The exposure scenarios include line-of-sight and non-line-of-sight propagation with the BS using equal gain transmission precoding at 3.5 GHz. Calculated channel parameters are discussed in comparison with the data available in the literature. The exposure in the phantom's head is evaluated in terms of the peak-spatial specific absorption rate averaged over a 10-g cube and referenced to the free-space time-averaged Poynting vector magnitude at the same location.

INDEX TERMS 5G, massive MIMO, EMF exposure.

I. INTRODUCTION

Massive multiple-input multiple-output (MIMO) is one of the most promising candidates as a 5G communication technology. First introduced in [1], it offers an unprecedented increase in spectral efficiency of a wireless link. It is achieved by equipping the base station (BS) with a large number of antennas compared to the number of simultaneously served users. The user equipment (UE) is a single antenna device. The BS estimates the propagation channel through receiving up-link pilots. This channel-state information (CSI) is used at the BS to preco de the signal it transmits, maximizing the desired signal strength at the receivers while minimizing interference. This is achieved by selecting the phases and amplitudes at the BS antennas (*precoding* them) such that their signals are combined constructively at the intended receivers and undergo a destructive interference at the other receivers. Various precoding strategies were devised and analyzed in [2]. The propagation environment and the precoding scheme used at the BS are the major factors influencing the electromagnetic field (EMF) distribution (Poynting vector) in vicinity of the receivers during the operation of a massive MIMO system.

Recently conducted theoretical studies were focused on the assessment of the realistic maximum power density levels and compliance boundary size. In [3], analytical expressions were used to describe the statistical properties of the massive MIMO operation and in [4], the 3GPP stochastic channel model was involved. In both works the line-of-sight (LOS) scenario was studied as yielding worst-case human exposure and operation of the massive MIMO system was reduced to *beamforming*.

However, in a non-line-of-sight (NLOS) scenario such approach might no longer be feasible. As there is no direct

The associate editor coordinating the review of this manuscript and approving it for publication was Mithun Mukherjee.

path between the BS and UE, forming conventional 'beams' is not beneficial as the signal gets attenuated by obstacles. Instead, the BS exploits the knowledge of the channel and allocates its power to multi-path components. High spatial multiplexing gain, typical for a massive MIMO transmission, results in sharp power density peaks confined to a narrow spatial region in proximity of the UE's terminal.

This paper presents a numerical approach for the evaluation of realistic EMF exposure to a massive MIMO BS downlink transmission in terms of localized specific absorption rate (SAR). This has never been done up to now, to the best of the authors' knowledge. It combines ray-tracing (RT) for deterministic geometry-based propagation calculation and the finite-difference time-domain (FDTD) method to assess exposure of a realistic human phantom.

Comparing LOS and NLOS modes of operation of a massive MIMO system could give insights into realistic exposure conditions.

In this paper, models of an indoor industrial environment are studied. It is envisioned that factories of the future will be equipped with multitudes of autonomous robots and human workers, all of which will require fast and reliable wireless connection. A single massive MIMO BS could potentially provide the needed service due to low path-loss (PL) exponent and rich scattering in such scenarios [5].

Recent measurement campaigns performed with massive MIMO test-beds [6] in indoor environments report its distinctive features: multi-user consistency, spherical wavefronts, and non-stationarity across the BS array. Current stochastic MIMO channel modeling frameworks, e.g. COST 2010 [7] and QuaDRiGa [8], do not account for these effects. Although possible extensions were proposed [9], [10], they are yet to be experimentally validated [11]. On the other hand, geometry-based massive MIMO channel modeling using the RT method complemented with the uniform theory of diffraction (UTD) has been reported to reproduce the aforementioned effects in both indoor [12] and outdoor environments [13].

The paper is organized as follows. In Section II, we explain the proposed numerical approach in detail, estimate the algorithmic complexity of the methods involved and the limits of their applicability. We also estimate the numerical error of our method. Section III presents the results obtained in a model case of industrial indoor environment. Time-averaged free-space Poynting vector magnitude and SAR in a heterogeneous human phantom are assessed. It also contains the discussion of the results with respect to the existing exposure guidelines.

II. MATERIALS AND METHODS

In this section, we explain the numerical approach. First, a high-level overview is given, where all steps involved are shown, and their connections are explained. Then, for each step, we elaborate the details. An example of its application is given for a model environment.

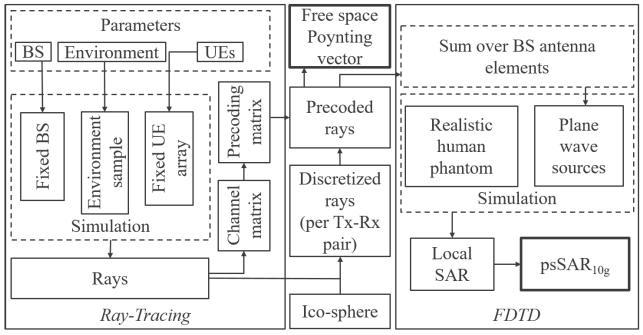

FIGURE 1. Numerical pipeline scheme. Ray-tracing, FDTD and the interface between them are shown.

A. NUMERICAL PIPELINE

A block-diagram of the proposed method is depicted in Figure 1. It can be conveniently viewed as consisting of two components: RT and FDTD. The hybridization of these two methods was first introduced in [14], where it was used for indoor wireless propagation prediction; the results were compared to the measured data, showing good agreement and superiority in precision over pure RT. The same approach was next applied to the human exposure assessment to conventional single-antenna BS in an urban macrocell in [15]. The results demonstrated the significance of the ''accurate modeling of the environment in which the exposure takes place''. Peak-spatial SAR averaged over 10g ($psSAR_{10g}$) was reported to increase around two times with reflections from a nearby wall taken into account. Inclusion of the propagation environment in the simulation is expected to have even stronger effect on exposure produced by a massive MIMO BS.

An extensive study [16] based on sets of single-plane wave FDTD simulations with adult heterogeneous human phantoms reported $psSAR_{10g}$ relative variation of around 300% with respect to the direction-of-arrival (DoA) of a plane wave. Therefore, a realistic modeling of the EMF-exposure should account for the expected DoA relative to the exposed subject. One way to achieve this is to utilize known DoA distribution for a particular type of environment when assessing the exposure statistically [17].

However, for a massive MIMO system directional information at the receiver side per BS antenna and inter-antenna correlation should as well be accounted for. These are often characterized via the notion of a *cluster* of scatterers, which is associated with a group of closely spaced DoAs. A cluster can be described with its DoA and relative power distributions. In proposed stochastic models of the massive MIMO channel, a widely used approach is to generate cluster parameters according to appropriately chosen distributions. Whether a cluster is shared between two BS antennas is given by a probability function.

As the input of a RT simulation is a geometrical model of an environment (see Figure 1), the RT approach has the

following advantage over stochastic models: all the channel information is extracted from the environment model, rather than being sampled stochastically.

The choice of distribution parameters in a stochastic model is equivalent to the definition of the RT simulation domain. We further discuss this in the analysis of the RT results.

We generate the geometry for RT simulations stochastically, described with a set of parameters.

The directional information of the incidence at the UE is *spatially consistent*. Scatterer clusters emerge naturally as the strongest propagation paths, between the BS and a UE. Importantly, RT calculates DoA per individual BS antenna element based on the shape of the antenna array, its orientation in space, etc. Power distribution, phase, and time-delay of the incident rays are calculated from the length of the propagation paths (path loss), possible reflections, transmissions (Fresnel equations) and diffractions a ray undergoes during its propagation (Figure 1, left).

Antenna radiation patterns are easy to incorporate into RT simulations, as it only requires scaling of the incident power with respect to direction of departure (DoD) at the transmitter and DoA at the receiver; it can be done as a postprocessing step of simulation results.

B. RAY-TRACING SIMULATION

We use REMCOM Wireless InSite software for RT simulations in this study. A RT simulation is intrinsically narrowband, as far as propagation is frequency-dependent. Given that the BS terminals are excited with a sinusoidal signal at frequency f_c, the ray-tracer calculates the channel transfer function between n^{th} BS antenna (Tx) and k^{th} UE (Rx) as

$$h_k^n = \sum_{r=1}^{s(k,n)} p_r \exp(-2\pi i f_c \tau_r), \tag{1}$$

where $s(k, n)$ is the total number of paths found between n^{th} Tx and k^{th} Rx points, p_r is the complex-valued impulse response through the r^{th} path and τ_r is the time-delay of the r^{th} path. Evaluating (1) for each Tx-Rx pair yields the frequency-specific channel matrix $\mathbf{H}(f_c)$ (Figure 1). Obtaining full channel matrix requires calculation of $\mathbf{H}(f)$ at every sub-carrier frequency utilized by a massive MIMO system. Further in the paper we focus on simulations at a single carrier frequency of 3.5 GHz.

The channel Gram matrix is commonly used for analysis of a massive MIMO system performance and given by

$$\mathbf{G} = \mathbf{H}^H \mathbf{H}. \tag{2}$$

It is a positive-semidefinite matrix of dimensions $K \times K$, where K is the overall number of simultaneously served UEs. Its k^{th} diagonal element is proportional to the power received by the UE#k, and the magnitude of its element with indices ij is proportional to the interference between i^{th} and j^{th} UEs.

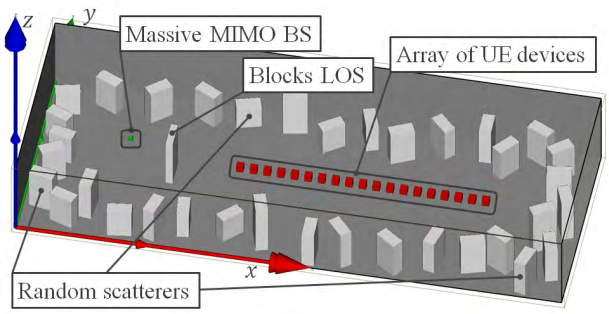

FIGURE 2. A sample of the environment in a ray-tracing simulation. Floorplan has the dimensions of 40 m×20 m×5 m. The floorplan and Tx-Rx arrangement is fixed, while cuboid scatterers are generated independently for each sample.

1) MODEL OF THE ENVIRONMENT

The ray-tracing simulations were done the in the indoor environment shown at Figure 2. The floor-plan is a 40 m×20 m×5 m rectangular room. A dielectric material with parameters $\varepsilon_r = 7$, $\sigma = 1.5 \cdot 10^{-2}$ S/m was assigned to its walls, floor and ceiling (concrete material model).

Scatterers are placed along the perimeter of the room, no more than 3 m away from the walls, distributed in the xy-plane with the Poisson Disk sampling algorithm [18]. The Poisson Disk sampling algorithm assures that the scatterers do not intersect and distributes them evenly inside the bounded region. The scatterers are cuboids of fixed width and length (2 m×0.5 m) and height sampled uniformly in the range from 2 m to 3 m. Each scatterer is independently rotated around the vertical axis, through the object's center, at an angle sampled uniformly in $[0, 2\pi)$.

Figure 2 shows the location of the massive MIMO BS (green) and a linear array of receivers (red). The center of the BS array is located at $x = 7$ m, $y = 10$ m, $z = 4$ m in the coordinate system depicted in Figure 2. The BS consists of 36 vertically polarized isotropic radiators arranged in a planar 6-by-6 array in yz-plane with a uniform 1λ (approx. 86 mm) spacing between the elements. All elements of the array are fed with equal power, such that the total radiated power of the BS is 1 W. In this study, we do not assign individual antenna patterns to the BS elements in order to simplify the analysis of the results.

Nineteen UEs are arranged in a linear array with equal 1 m spacing spanning from 15 to 33 m along the x-axis. All UEs are elevated at equal height of 1.5 m (along the z-axis). A receiver is modeled with a single vertically polarized isotropic antenna.

In addition, one cuboid of size 2 m×0.2 m×4 m can be placed at the fixed location (x =10 m, y =10 m), blocking the direct path between the BS and the array of receivers (see Figure 2). We further refer to the setup where the cuboid is present as the *NLOS* scenario and the setup without the cuboid as the *LOS* scenario.

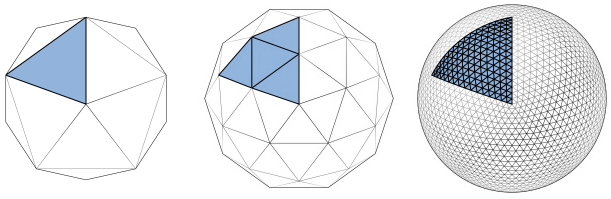

FIGURE 3. Icosahedral triangulation of a sphere of frequency i. (a) $i = 1$, 20 faces (Icosahedron); (b) $i = 2$, 80 faces; (c) $i = 16$, 5120 faces.

2) DISCRETIZATION OF INCIDENT RAYS

A ray $r_{n,k} = \{f_c, \mathbf{n}, \mathbf{E}, \mathbf{H}\}$ in the RT method is described by the frequency f_c, DoA vector $\mathbf{n}$ of the plane wave it represents (a unit vector *opposite* to the direction of the plane wave propagation), complex amplitudes of its electric and magnetic fields $\mathbf{E}, \mathbf{H}$, and indices of a Tx-Rx pair (n, k) it is calculated for.

Many modern FDTD software tools feature a functionality to create plane wave sources. We use this feature available in EM-FDTD solver of Sim4Life v4.0 (ZMT, Zürich, Switzerland) and model an incident ray as a plane wave source propagating in the entire domain.

The simulation time is nearly linearly proportional to the total number of plane wave sources in it. Moreover, the number of rays incident at the specific point is also proportional to the number of the antennas at the BS, as each antenna is traced independently.

The overall number of rays that reach a particular UE depends on the environment, Tx-Rx positions, and attenuation threshold, after which a ray is discarded; e.g., in the studied environment with the power threshold of -50 dB and source ray spacing of 0.02°, on average around 220 rays per Tx-Rx pair were observed, resulting in approximately $8 \cdot 10^3$ rays per UE.

Such large number of plane waves in a simulation leads to a long run time and renders it impractical to conduct the simulations in extensive sets of environment samples. It is computationally beneficial to combine rays with closely aligned propagation directions before introducing them into the FDTD domain.

To reduce the number of plane waves in an FDTD simulation, hence, decreasing simulation time, we perform DoA discretization of the incident rays at each UE. We define a grid on a unit sphere and use the normal vectors of its elements to approximate DoA of the rays calculated with the RT method. If the set is sufficiently large and covers all DoA space in a uniform manner, the error introduced by this procedure is expected to be small for any distribution of DoA of the incident rays. This procedure allows to add up the complex amplitudes of the discretized rays having equal DoAs, decreasing the total number of plane waves in the FDTD simulation (and proportionally decreasing CPU time).

We use a geodesic spherical grid based on subdivision of an icosahedron. By subdividing every edge of the icosahedron into i segments, triangulating its faces and projecting newly created vertices into the unit sphere, an icosahedral triangulation of a sphere (icosahedral sphere, ico-sphere) of frequency i is generated. The angle between any two adjacent triangles (a dihedral angle) of an ico-sphere is nearly constant, which makes its surface a largely isotropic spherical grid.

For each ray the calculated DoA vector $\mathbf{n}$ is replaced by $\tilde{\mathbf{n}}$, being the outer normal of the ico-sphere face $\mathbf{n}_i$ with the maximal orthogonal projection onto $\mathbf{n}$,

$$\tilde{\mathbf{n}} = \arg\max_{\mathbf{n}_i}\{(\mathbf{n}, \mathbf{n}_i)\}. \tag{3}$$

To estimate the error introduced by the discretization procedure, let us consider two plane waves with wave-vectors $\mathbf{k}_1$ and $\mathbf{k}_2$, such that $|\mathbf{k}_1| = |\mathbf{k}_2|$ and $\angle(\mathbf{k}_1, \mathbf{k}_2) \leq \beta_i$, where β_i is the largest dihedral angle of an ico-sphere of frequency i. Then the shortest distance between two neighboring interference pattern maximas (*fringe spacing*) is given by $d_i = \lambda / \sin\beta_i$ [19]. Table 1 presents values of d_i calculated for $i \leq 16$. Starting from $i = 4$, the fringe spacing becomes larger than the expected domain size. We use this as a starting value in the following numerical evaluation of the associated error.

TABLE 1. Distance between interference peaks for different ico-sphere frequencies.

i	Face count	$\angle(\mathbf{k}_1, \mathbf{k}_2)$, [°]	d_i, [λ]	d_i, [m]
1	20	41.81	1.5	0.12
2	80	18.02	3.23	0.26
4	320	7.8	7.37	0.59
8	1280	3.19	17.96	1.44
16	5120	1.41	40.73	3.26

To numerically estimate the error introduced by DoA discretization in the simulated environments, we compare the time-average power flux density $\mathbf{S}$ calculated from the full set of rays obtained with the RT method and their discretized approximations $\mathbf{S}_i$ for icosahedral sphere frequencies i listed in the Table 1. We integrate the absolute difference between x-components of $\mathbf{S}$ and $\mathbf{S}_i$ and their mean value over a 190 mm × 240 mm rectangle A in the yz plane. The ratio of two is used to measure the error

$$\Delta_i = \frac{\int_A |S_x - S_{x,i}|}{\int_A |S_x|}. \tag{4}$$

The area of integration is the projection of the phantom's head bounding box on the yz plane (wich is the phantom's coronal plane). As such, Δ_i approximates the relative error of the total power incident at the phantom's head along the x-axis when discretizing the rays using the ico-sphere of frequency i (see Fig. 5). We calculated Δ_i for 100 samples of the environment in Figure 2 with the NLOS scenario; its value averaged over all samples and all UE locations along with its standard deviation σ as a function of i are shown at Figure 4.

Mean Δ_4 approximately equals 20% and for some samples exceeds 30%. However, Δ_i falls rapidly as i increases. Mean Δ_{16} was found to be around 5.5% with its value staying

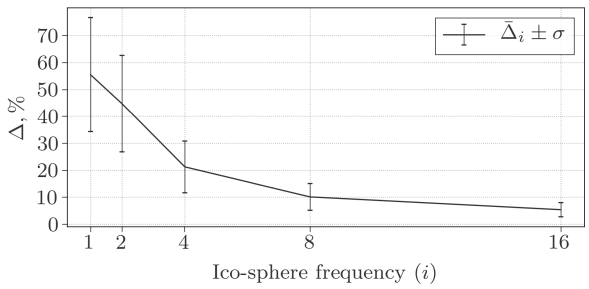

FIGURE 4. Relative error of the total power incident along the x-axis. Sample average and standard deviation over 100 RT simulations are shown.

below 12% for all samples. Numerical uncertainty of exposure assessment caused by the finite FDTD grid resolution is reported to be around 10% for the grid step of 2 mm and frequencies below 5 GHz [20]. Thus ico-sphere of frequency 16 was considered to provide a sufficiently accurate approximation for the incident field.

In the studied environment, the overall number of the discretized rays for a given UE rarely exceeded 250, which reduced the FDTD simulation run-time by a factor of 30. This approximation was further used in FDTD simulations with a realistic human phantom.

C. FDTD SIMULATIONS

Sim4Life FDTD software was used for the simulations described in this section. The simulation domain is shown in Figure 5. The EMF-exposure is assessed using the ViP v.3.1 Duke heterogeneous human phantom [21]. psSAR_{10g} is used to measure the exposure as highly focused energy distributions are expected (hotspots).

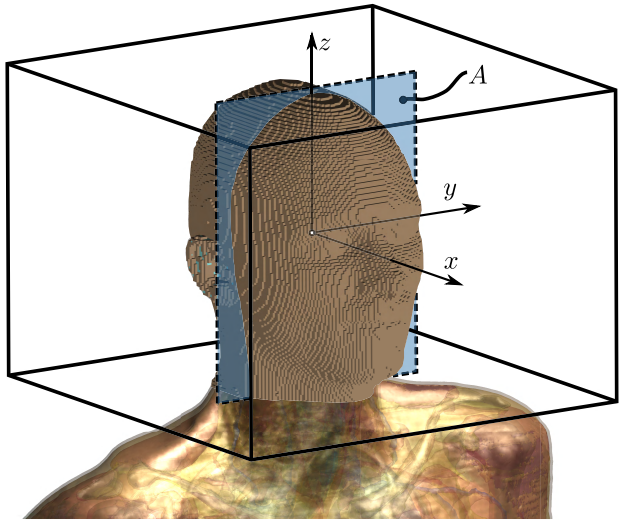

FIGURE 5. A computational domain of the FDTD simulation. Domain boundaries are shown with solid black lines. Voxels of the ViP v.3.1 Duke phantom's head, included into the domain, are shown. Dashed line depicts to boundary of the integration surface A (shaded area) in (4).

The center of the domain is coincident with the position of the UE, where the exposure is being assessed. The UE is assumed to be a mobile phone in a typical usage scenario close to the head. Accurate modeling of the usage scenario requires positioning the phantom inside the domain preserving its arrangement relative to the UE. Here we use a simplified approach by centering the phantom's head at the position of the UE (center of the domain).

In addition, we only include the phantom's head into the FDTD domain to reduce the computational demand. The domain dimensions were set to 300 mm $\times$ 300 mm $\times$ 250 mm to fully enclose the phantom's head.

The discretization step did not exceed 2 mm which resulted in more than 40 grid steps per wavelength at 3.5 GHz. The total number of voxels was around 3.3×10^6.

III. RESULTS

A. MASSIVE MIMO CHANNELS

To evaluate the massive MIMO performance in the proposed environment we investigate the channel matrices and compare their properties with those of the theoretical i.i.d. Rayleigh channels.

Figure 6a depicts a channel Gram matrix, which channel response was modeled with independent sampling from a circularly symmetric Standard Normal distribution, according to the Rayleigh fading model. The dominance of its diagonal elements is conditioned by the law of large numbers, as any off-diagonal element is the average of a large number (number of the BS antennas N) of random variables with zero-mean. At the same time, any diagonal element is the square of the absolute channel impulse response, and proportional to the power received by the corresponding UE.

Figure 6c shows an example of a channel Gram matrix calculated with the RT method in the NLOS scenario. Relative magnitude of a diagonal element decreases with increasing UE index. This is the result of the PL, as the distance from the BS to the corresponding UE increases.

The arithmetic mean of the channel Gram matrices obtained in 100 NLOS environment samples are depicted in Figure 6d. Comparing Figure 6c and Figure 6d, one can see that the channel impulse response is indeed uncorrelated between independently generated environment samples. The correlation between channels (off-diagonal elements at Figure 6c) occasionally reaches the order of magnitude of the signal (diagonal elements), but vanishes on average.

LOS channels exhibit much higher correlation (Figures 6e and 6f) between farther spaced receivers compared with NLOS, which is explained by the shared direct path component. The correlation further increases when strong scatterers are shared between UEs, as illustrated at Figure 6e for UE#2 and UE#3, in which case the channels become nearly identical up to a constant phase shift. On average the diagonal elements dominate, though the observed correlation is higher than the one of NLOS or i.i.d. Rayleigh channels.

The quantitative analysis of the channel is often performed using the channel matrix singular value spread (SVS) $\kappa(\mathbf{H})$ [22] and channel Gram matrix power ratio $\gamma(\mathbf{G})$ (MPR) [13].

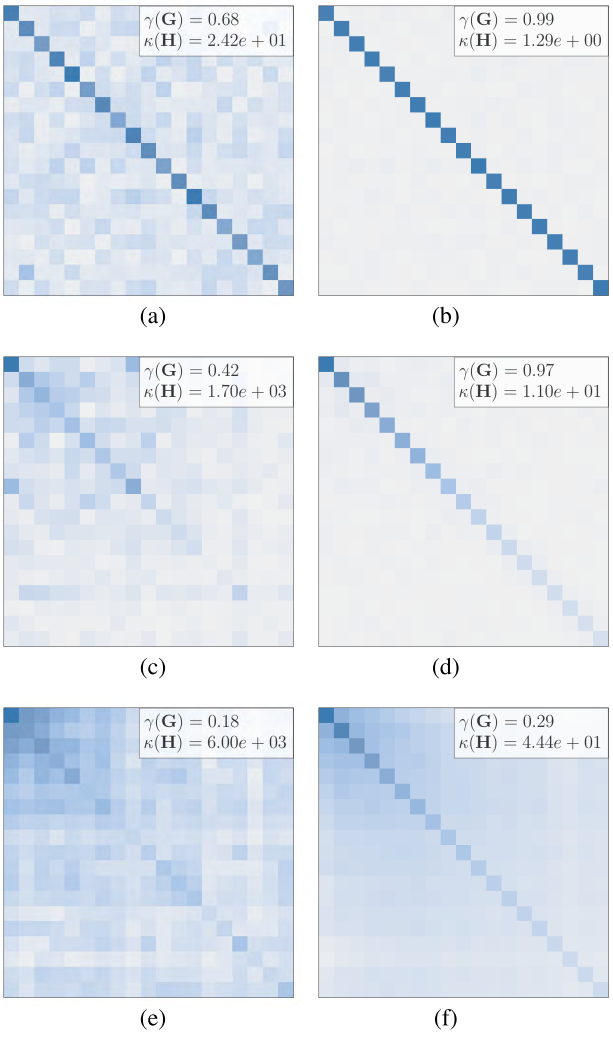

FIGURE 6. A comparison of normalized channel Gram matrices ($K = 19$, $N = 36$). (a): An example of i.i.d. Rayleigh channel model with $h_n^k \sim \mathcal{CN}(0, 1)$. (b): Average of 100 i.i.d. Rayleigh samples. (c): An example of NLOS scenario (see Figure 2). (d): Average over 100 NLOS environment samples. (e): An example of LOS scenario. (f): Average over 100 LOS environment samples. (a) i.i.d. Raleigh channels. (b) Avg. i.i.d. Raleigh. (c) NLOS. (d) Average NLOS. (e) LOS. (f) Average LOS.

$\kappa(\mathbf{H})$ is the ratio between the maximum and the minimum singular values of $\mathbf{H}$. SVS is the measure of correlation between the channel vectors: it equals to 1 for perfectly orthogonal channels (all singular values equal 1) and larger than one for non-orthogonal channels. $\kappa(\mathbf{H})$ close to 1 indicates that the channel exhibits *favorable propagation conditions* for the operation of a massive MIMO system.

$\gamma(\mathbf{G})$ is the ratio between the sum of squared absolute values of the diagonal elements of $\mathbf{G}$ and the sum of all its elements absolute values squared

$$\gamma(\mathbf{G}) = \frac{\sum_{i=1}^{K} |g_{i,i}|^2}{\sum_{i=1}^{K}\sum_{j=1}^{K} |g_{i,j}|^2}. \tag{5}$$

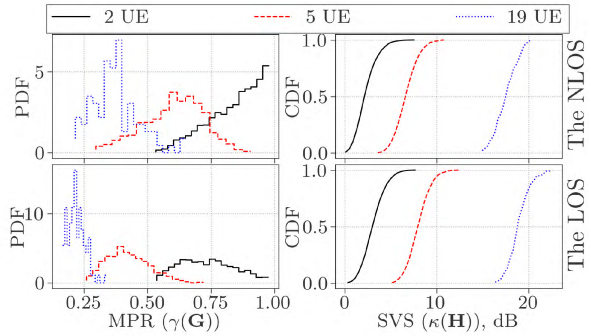

FIGURE 7. Probability density function of $\gamma(\mathbf{G})$ (left column) and cumulative distribution function of $\kappa(\mathbf{H})$ (right column) for 2, 5 and 19 active adjacent UEs. Results for the NLOS (top row) and LOS (bottom row) scenarios are shown.

$\gamma(\mathbf{G})$ is the portion of the electromagnetic energy that is focused at the intended receivers instead of interfering with other receivers. In i.i.d. Rayleigh channels $\gamma(\mathbf{G})$ tends to 1 and goes to 0 when a significant inter-channel correlation is present.

To evaluate the variation of $\kappa(\mathbf{H})$ and $\gamma(\mathbf{G})$ in the studied environment model (and quantify its suitability for the deployment of a massive MIMO system) we select all sub-arrays of n consecutive UEs from the original UE array and calculate the above quantities for 100 environment samples. Figure 7 depicts the sample probability density function (PDF) of $\gamma(\mathbf{G})$ and cumulative distribution function (CDF) of $\kappa(\mathbf{H})$ for $n = 2, 5$ and 19 (whole UE array) in LOS and NLOS scenarios. For larger n always a larger SVS is observed, in agreement with measurement results in [23] and the results of RT simulations in [13].

The NLOS scenario offers better propagation conditions compared with LOS, which agrees with [24]. This is expected, as in the LOS scenario all UEs are positioned along one straight line, which is also the strongest propagation path, i.e. the phase of the signal is correlated with its DoA for all receivers. However, the SVS rarely exceeds 10 dB in both scenarios for $n \leq 5$, which means that the BS is capable at providing a good service to up to 5 closely spaced UEs. Channels to more sparsely distributed users tend to be less correlated. This allows to conclude that the proposed environment model is well-suited for the deployment of massive MIMO and the average EM-field incident at the UEs can be treated as realistic.

B. POWER FLUX DENSITY FOCUSING IN FREE SPACE

Here we examine the behavior of the time-averaged power density flux in free space in the neighborhood of the UE to which the transmission occurs. A simple case when the BS transmits to a single-user only was studied. This is a potential worst case exposure-wise (for EGT precoding scheme), as the BS attempts to focus all the available power at a single user position rather than spreading it between multiple locations in a multi-user case.

Strictly speaking, the results of the RT simulation are only valid at the point in space that is coincident with the position of the assessed UE. However, spatial distribution of the EM-field in proximity of the point is determined by the phase-amplitude relation of the incident plane waves if their DoA variation close to that point is sufficiently small.

To examine to which extent this assumption holds, we performed 100 RT simulations in the NLOS scenario (Figure 2) with a linear array of densely spaced (10 mm separation) receivers spanning for 0.5 m along the x-axis at 20 m distance from the BS. On average, correlation of the incident rays power as a function of DoA was found to be above 60% for the UE separation distance less than 200 mm. Therefore, we further examine EM-field distributions in a finite space region.

In this and following sections we apply Equal Gain Transmission (EGT) scheme [25] to precode the discretized rays. The EGT is realized by setting the phase of the signal at every BS antenna element opposite to the phase of the received signal at the terminal of the UE to which the transmission is intended, while maintaining the amplitude of the signal equal at all BS antennas. Using the definition of the channel matrix element (1), we obtain EGT-precoded complex E-field amplitude of the j^{th} ray incident at the k^{th} UE from the n^{th} BS antenna as

$$\hat{\mathbf{E}}^{j}_{n,k} = \mathbf{E}^{j}_{n,k} \exp(-i \arg(h^{n}_{k})). \tag{6}$$

Then the E-field at the point $\mathbf{r}$ in proximity of the k^{th} user is found taking the sum over all rays and BS antennas

$$\mathbf{E}^{EGT}_{k}(\mathbf{r}) = \sum_{n=0}^{N} \sum_{j} \hat{\mathbf{E}}^{j}_{n,k} \exp(-i\mathbf{k}_j \mathbf{r}), \tag{7}$$

where $\mathbf{k}_j$ is the wave-vector of the j^{th} ray. Equations for the magnetic field are obtained by substituting $\mathbf{H}$ for $\mathbf{E}$ in (6) and (7).

Time-average power density flux is the real part of the EM-field Poynting vector [19]

$$\mathbf{S}^{EGT}_{k}(\mathbf{r}) = \mathrm{Re}\left(\frac{\mathbf{E}^{EGT}_{k} \times \mathbf{H}^{*EGT}_{k}}{2}\right). \tag{8}$$

We evaluated (8) on a uniform rectilinear two-dimensional grid in the xy plane at $z = 0$ constructed for all UEs in the LOS and NLOS scenarios for 100 environment samples.

Figures 8a and 8b show spatial distributions of $\mathbf{S}^{EGT}_{k}(x, y)$ averaged over UE locations and environment samples for LOS and NLOS scenarios respectively. They illustrate the average power flux density gain in the studied environment model that the BS delivers. The BS is located in the negative x-axis direction at $y = 0$. In both cases, the maximum power density is observed in the center of the domain (UE antenna terminal). This is the effect of focusing achieved by precoding of the transmission by (6): on average the signal arrives at the receiver having zero-phase and adds-up coherently. It is important to emphasize that not all the propagation paths combine coherently at the center. The impulse

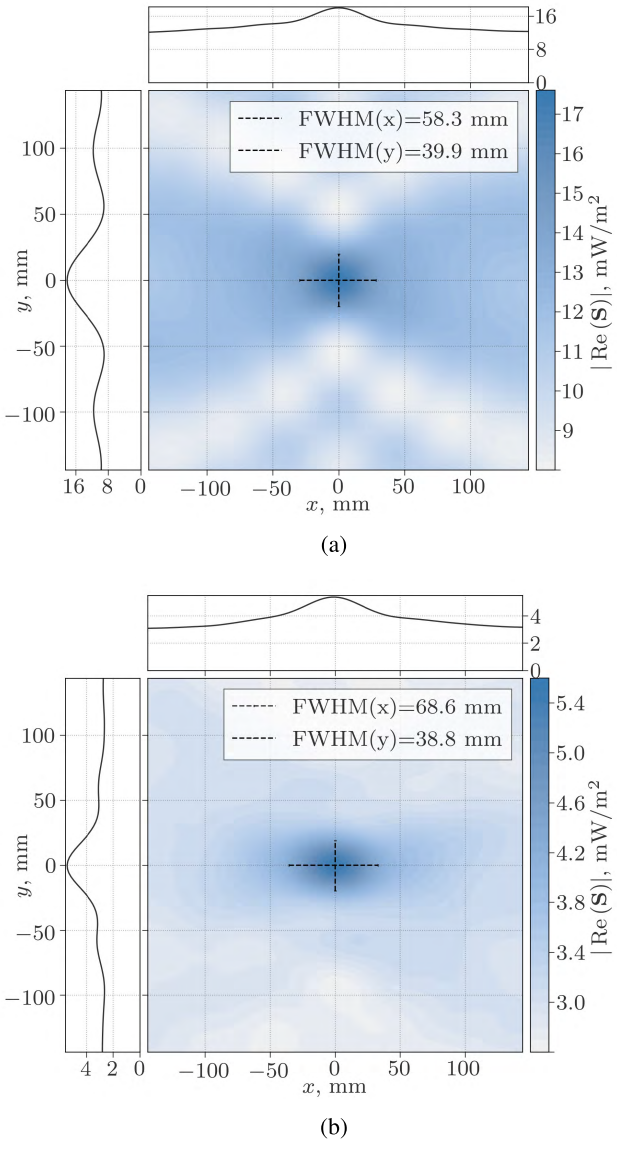

FIGURE 8. Spatial distribution of the time-average power flux density in the *xy*-slice through the location of the UE, averaged over all UEs in 100 environment samples. Total BS transmitted power is normalized to 1 W. (a): The LOS scenario; (b): The NLOS scenario. (a) The LOS scenario. (b) The NLOS scenario.

response from every BS antenna is constituted by multiple propagation paths, phase relation between which is fixed and determined by the environment. It is by coherently combining instantaneous field distributions produced by multiple antennas, that the focusing is achieved. The less correlated the signal response between the antennas is (that is the less alike these individual field distributions are) the sharper the field enhancement at the receiver can be produced.

In this regard the difference between LOS and NLOS scenarios is evident. In the LOS scenario the strongest propagation paths, being nearly collinear with the positive x-axis direction, have narrow angular spread, which results in interference patterns with wide maxima. In contrast, when direct paths are obstructed, incident power has a more uniform and

wide angular spread; this results in higher angular diversity in the incident rays (larger ''aperture'') and sharper focusing along y-axis, as can be seen at Figure 8b.

On the other hand, in the NLOS scenario the strongest propagation paths are blocked, which results in more than 3 times lower absolute average of $\mathbf{S}^{EGT}(0, 0)$.

To compare the focusing effect in both scenarios we calculate full width at half maximum (FWHM) of the spatial distribution relative to the background, along x and y axes, as shown at the top and left side of Figures 8a and 8b.

For LOS and NLOS we found FWHM(y)$\simeq$39 mm or 0.45λ and FWHM(x)$\simeq$63 mm or 0.74λ respectively. We use the average of two values as the focusing performance indicator, which in this case approximately equals 51 mm or 0.59λ.

Another measure of focusing performance is the power density gain reached with the EGT precoding relative to power density of non-precoded BS transmission. This aspect and spatial variation of the power density at a larger scale is discussed in more details in the following sections.

C. SPATIAL DISTRIBUTION OF SAR

We use psSAR_{10g} to study localized exposure in the head of the heterogeneous phantom model as described above. Due to a highly focused EM-field distribution in proximity of the head, peak-spatial SAR averaged over 10-gram cube is a suitable quantity for the EMF-exposure estimation. 10-gram averaging cube and the maximum permissible psSAR_{10g} are standardized by the International Commission on Non-Ionizing Radiation Protection (ICNIRP) in [26].

The FDTD simulations are performed for two rotation angles of the phantom (0° and 90°) relative to the BS were conducted for each environment sample. As discussed in Section II, psSAR varies significantly with the incidence direction; exposure from the back of the head (0° rotation) and exposure from the side (90° rotation) are examined to study this effect.

Figures 9a and 9b depict the distributions of psSAR_{10g} in a horizontal slice of the phantom's head, averaged over 19 UEs in the LOS scenario, exposed from the back and from the side respectively. When exposed from the back the maximum psSAR_{10g} value is almost two times lower compared to the one found with exposure from the side setup. This is largely explained by the irregular structure of the ear, where the peak-cube is a almost always found in the side-exposure case, which agrees with a single-plane wave exposure studied in [16]. More generally, this effect can be attributed to the fact that in the LOS scenario most of the radiation is incident from the half-space where the BS resides. Location of the peak-cubes are on average aligned with the direction to the BS in LOS for both angles of rotation, which also supports the argument above. Most of the psSAR_{10g} cubes are found in the top of the head when the phantom is exposed from the back, which is why the slice depicted on Figure 9a is located higher than on the others of Figure 9.

Distributions of psSAR_{10g} for two angles of the phantom's head rotation averaged over 10 environment samples and all UE positions in NLOS scenario are shown on Figures 9c and 9d. As mentioned in Section III-B, NLOS scenario results in a broader distribution of DoA in the incident rays. Thus the location of the peak-cube in the phantom's head is less correlated with the direction to the BS (or the angle of rotation of the head) compared with the LOS scenario. For both the 0° and 90° degrees rotation in Figures 9c and 9d, most of the peak-cubes were located in the ears.

Another effect of the wider DoA spread is that the power deposition in the head gets distributed more evenly over multiple regions. As a result, the maximum psSAR_{10g} normalized to the power density in the free-space hotspot (obtained in the same exposure conditions) drops on average compared to that in the LOS case.

D. LARGE-SCALE VARIATION OF THE LOCALIZED SAR

In this section we evaluate the power density in free space and psSAR_{10g} in the phantom's head as a function of the UE distance from the BS.

1) LOS

Results for the LOS scenario are given in Figure 10a. The graph at the top depicts the sample average of the free-space power flux density, calculated for 100 environment samples.

$\mathbf{S}_{EGT}$ and $\mathbf{S}_{rand}$ are the free-space time-averaged Poynting vectors evaluated at the location of the UE when the BS antennas transmit with EGT-precoded and with independent random (in $[0, 2\pi)$) phases respectively. The ratio $|\mathbf{S}_{EGT}|/|\mathbf{S}_{rand}|$ is the EGT-precoding gain in terms of the time-averaged power density. It is fairly stable over the distance; varying between 13.2 and 15.5 dB, its average approximately equals 14.4 dB. It is also interesting to compare these values with the power density calculated with the free-space path loss model $\mathbf{S}_{f.s.}$, shown with a dashed blue line. It is calculated using Friis free-space transmission formula [25] for a single isotropic radiator with the total power of 1 W as the BS. Everywhere $\mathbf{S}_{rand}$ is larger than $\mathbf{S}_{f.s.}$ with their ratio increasing from around 3.9 to 6.9 dB as the distance to the BS increases. This can be explained by the presence of the PEC scatterers which reflect EM-energy and channel it through the environment, instead of absorbing it. This is confirmed by the extensive measurement campaigns [27] carried out in industrial indoor environments, which report PL exponent less than 2 in the studied frequency range.

The graph at the bottom of Figure 10a depicts the maximum psSAR_{10g} averaged over 10 LOS environment samples with the phantom exposed from the back (0° rotation, blue line), side (90° rotation, red line) and 5^{th} - 95^{th} percentile range taken from the distribution of all 20 exposure values (shaded region). At all UE locations exposure from the side was found to be higher than from the back by a factor of 2.6 on average. Overall, the average maximum psSAR_{10g} value is closely proportional to $\mathbf{S}_{EGT}$ in the hotspot with the proportionality factor varying from around $2.7 \cdot 10^{-2}$ m^2/kg to $4.4 \cdot 10^{-2}$ m^2/kg.

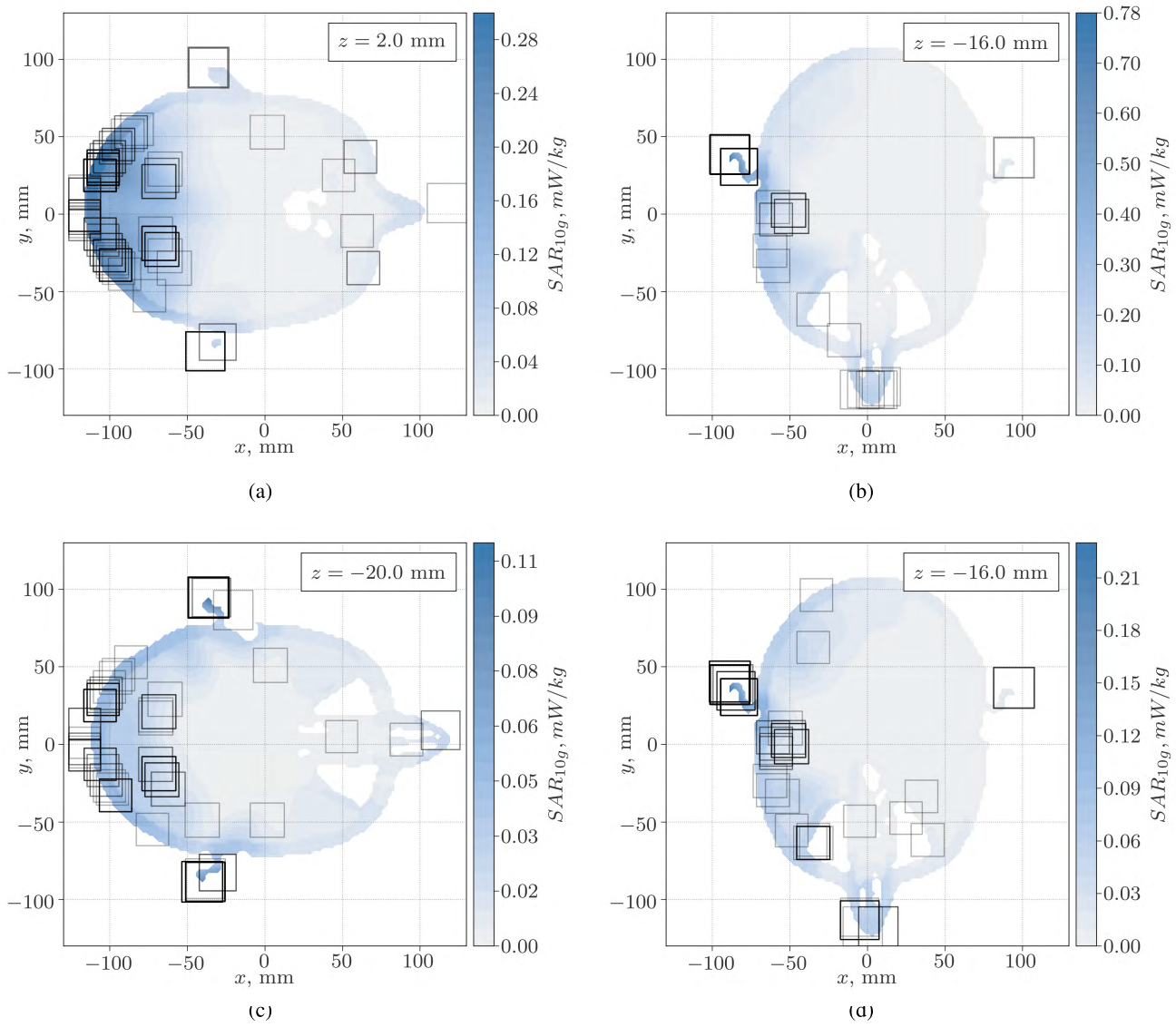

FIGURE 9. Color shows SAR_{10g} distribution, normalized to 1 W BS power and averaged over all 19 UEs in 10 environment samples; z coordinate of the slice is coincident with the maximum average SAR_{10g} and indicated in the top-right corner; black squares depict peak-cubes in each exposure sample projected onto the slice. (a): Exposure from the back in the LOS scenario; (b): Exposure from the side, LOS; (c): Exposure from the back, NLOS; (d): Exposure from the side, NLOS. (a) Exposure from the back, LOS. (b) Exposure from the side, LOS. (c) Exposure from the back, NLOS. (d) Exposure from the side, NLOS.

2) NLOS

Power flux density magnitude in the NLOS scenario is shown at Figure 10b (top) (100 samples). The precoding gain in the NLOS scenario varies slightly more with distance and has a nearly equal absolute average value of around 14.3 dB, compared with LOS. The former is the result of a more rich scattering environment which NLOS provides, as was mentioned in the previous section.

Another interesting effect is the increased relative variation of EGT-precoded power density $\mathbf{S}_{EGT}$ for all UE positions. This is expected: the signal variation is related to the geometry variation across the environment samples. Randomly generated scatterers play a less significant role in the non-obstructed propagation (LOS), as the direct component is constant and shared among all samples.

The comparison of the large-scale fading with the free-space model shows a larger PL in the NLOS. This is the effect of shadowing by the LOS-blocking scatterer (see Figure 2). It is interesting that UEs at an intermediate distance from the BS experience less shadowing; it might indicate that the signal is more likely to reach those UE locations through less interactions with the environment (e.g. with only 1 reflection).

At the bottom of Figure 10b, the $psSAR_{10g}$ variation with distance in 10 NLOS environment samples is depicted. It was found to be around 3.5 times lower than that of the

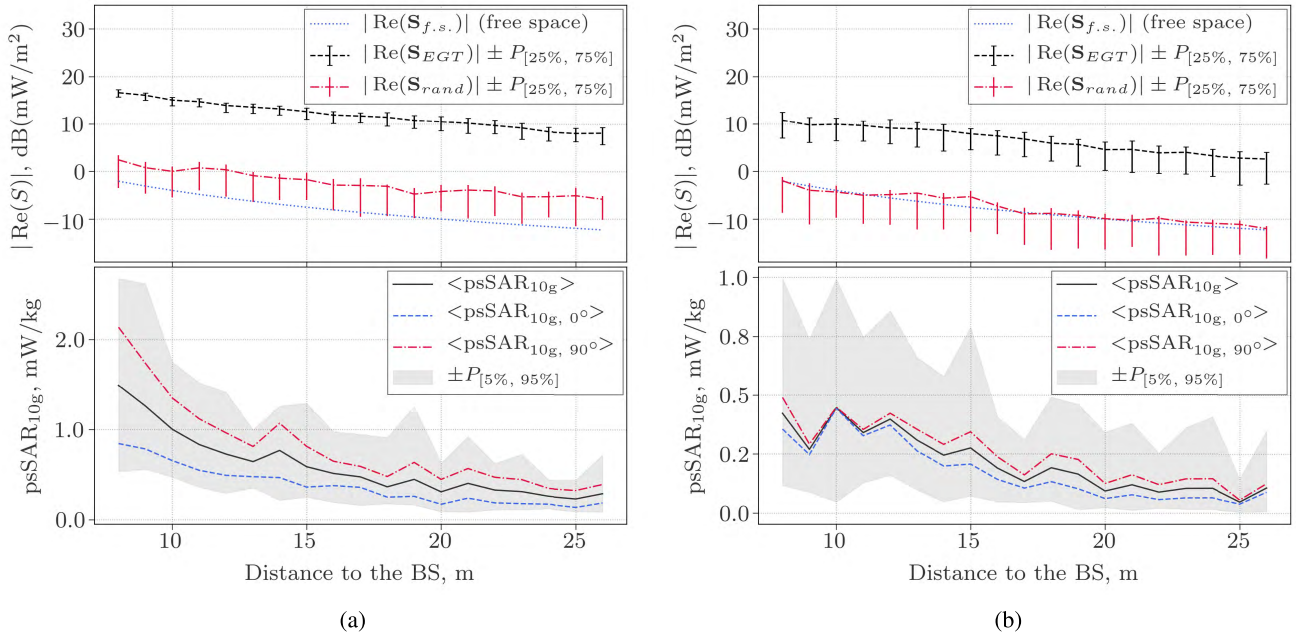

FIGURE 10. As a function of distance to the BS. Top row: time-averaged power flux density at the locations of the UE. Black dashed line shows EGT-precoded sample average and error-bars denote 25th - 75th percentile range; red dash-dotted line shows average power density with no precoding applied; blue dotted line gives a free-space path-loss reference. Bottom row: psSAR$_{10g}$ in the phantom's head. Black solid line shows average over 100 environment samples and 2 phantom rotation angles; blue dashed and red dash-dotted graphs show rotation-specific average values, for 0° and 90° rotation angles respectively; gray shaded area marks 5th - 95th percentile range. All values are normalized to 1 W BS total transmitted power. (a) The LOS scenario. (b) The NLOS scenario. (a) The LOS scenario. (b) The NLOS scenario.

LOS scenario. The relative difference between exposure from the back and from the side was found to be lower in NLOS than in LOS as a result of a less directive incidence. Exposure from the back is as well lower than from the side, though for some UE their average values are very close (e.g. at 10 and 25 m distance).

E. COMPARISON WITH THE GUIDELINES

From the evaluated normalized exposure, we now determine the power that the BS would need to transmit in order to violate the ICNIRP basic restrictions for the general population (2 W/kg [26]) at a given distance in the LOS and NLOS scenario, denoted as P_{LOS} and P_{NLOS} respectively.

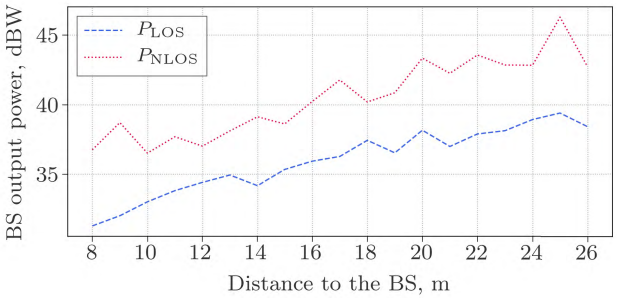

FIGURE 11. BS output power violating ICNIRP guidlines. Blue dashed line - the LOS schenario; red dotted line - NLOS.

Figure 11 presents P_{LOS} and P_{NLOS} as functions of distance to the BS. P_{LOS} increases from around 31 to 39 dBW nearly linearly with distance. P_{NLOS} has a slightly steeper trend line and on average exceeds P_{LOS} by 5 dB. As an example, at the shortest studied distance (8 m) this results in the BS transmitted power per antenna limits of around 35 W in the LOS scenario and around 110 W in the NLOS scenario, which is more than satisfactory for almost all indoor wireless communication systems.

IV. CONCLUSIONS

We presented a numerical framework that for the first time allows to estimate human EMF-exposure and localized absorption caused by a massive MIMO system. We applied the method to a generic model of an indoor industrial environment with a single massive MIMO BS. The calculated wireless channels were analyzed and the results were compared to the data available in the literature, showing good agreement. The gain of the system in terms of the time-average power flux density at the receiver antenna terminal was obtained when using EGT precoding at the BS. In the assumption of single-user transmission, exposure in terms of psSAR$_{10g}$ was assessed for users in LOS and NLOS propagation conditions at distances to the BS ranging from 8 to 26 m. Detailed results presenting psSAR$_{10g}$ distributions and peak-cube locations are discussed with respect to the exposure conditions. psSAR$_{10g}$ variation with distance to the BS was analyzed and compared to the power density observed in free space at the same location. Finally, maximum allowed powers of the massive MIMO BS were obtained in LOS and NLOS scenarios.

The introduced approach can be further extended to account for the individual radiation patterns of the elements in the massive MIMO array, more advanced precoding techniques and multi-user transmission scenarios. Other types of environments (e.g. outdoor) and topologies are to be studied. This remains to be the main focus of the future research.

REFERENCES

[1] T. L. Marzetta, "Noncooperative cellular wireless with unlimited numbers of base station antennas," *IEEE Trans. Wireless Commun.*, vol. 9, no. 11, pp. 3590–3600, Nov. 2010.
[2] F. Rusek *et al.*, "Scaling up MIMO: Opportunities and challenges with very large arrays," *IEEE Signal Process. Mag.*, vol. 30, no. 1, pp. 40–60, Jan. 2013.
[3] B. Thors, A. Furuskär, D. Colombi, and C. Törnevik, "Time-averaged realistic maximum power levels for the assessment of radio frequency exposure for 5G radio base stations using massive MIMO," *IEEE Access*, vol. 5, pp. 19711–19719, 2017.
[4] P. Baracca, A. Weber, T. Wild, and C. Grangeat, "A statistical approach for RF exposure compliance boundary assessment in massive MIMO systems," in *Proc. 22nd Int. ITG Workshop Smart Antennas (WSA)*, Mar. 2018, pp. 1–6.
[5] J. F. Coll, J. D. M. de Ojeda, P. Stenumgaard, S. M. Romeu, and J. Chilo, "Industrial indoor environment characterization—Propagation models," in *Proc. EMC Eur.*, York, U.K., Sep. 2011, pp. 245–249.
[6] A. Karstensen, J. O. Nielsen, P. Eggers, E. De Carvalho, M. Alm, and G. Steinböck, "Dual-user massive MIMO measurements at 3.5 GHz with bi-directional angular discrimination," in *Proc. 12th Eur. Conf. Antennas Propag. (EUCAP)*, 2018, p. 5.
[7] L. Liu *et al.*, "The COST 2100 MIMO channel model," *IEEE Wireless Commun.*, vol. 19, no. 6, pp. 92–99, Dec. 2012.
[8] S. Jaeckel, L. Raschkowski, K. Börner, and L. Thiele, "QuaDRiGa: A 3-D multi-cell channel model with time evolution for enabling virtual field trials," *IEEE Trans. Antennas Propag.*, vol. 62, no. 6, pp. 3242–3256, Jun. 2014.
[9] X. Gao, J. Flordelis, G. Dahman, F. Tufvesson, and O. Edfors, "MIMO channel modeling–extension of the COST 2100 model," in *Proc. Joint NEWCOM/COST Workshop Wireless Commun. (JNCW)*, 2015, pp. 1–10.
[10] A. O. Martínez, P. Eggers, and E. De Carvalho, "Geometry-based stochastic channel models for 5G: Extending key features for massive MIMO," in *Proc. IEEE 27th Annu. Int. Symp. Pers., Indoor, Mobile Radio Commun. (PIMRC)*, Sep. 2016, pp. 1–6.
[11] K. Zheng, S. Ou, and X. Yin, "Massive MIMO channel models: A survey," *Int. J. Antennas Propag.*, vol. 2014, Jun. 2014, Art. no. 848071.
[12] J. Weng, X. Tu, Z. Lai, S. Salous, and J. Zhang, "Indoor massive MIMO channel modelling using ray-launching simulation," *Int. J. Antennas Propag.*, vol. 2014, Aug. 2014, Art. no. 279380.
[13] D. Loschenbrand, M. Hofer, and T. Zemen, "Ray-tracer based channel characteristics for distributed massive MIMO," IRACON-COST, Feb. 2017.
[14] Y. Wang, S. Safavi-Naeini, and S. K. Chaudhuri, "A hybrid technique based on combining ray tracing and FDTD methods for site-specific modeling of indoor radio wave propagation," *IEEE Trans. Antennas Propag.*, vol. 48, no. 5, pp. 743–754, May 2000.
[15] P. Bernardi, M. Cavagnaro, S. Pisa, and E. Piuzzi, "Human exposure to radio base-station antennas in urban environment," *IEEE Trans. Microw. Theory Techn.*, vol. 48, no. 11, pp. 1996–2002, Nov. 2000.
[16] T. Uusitupa, I. Laakso, S. Ilvonen, and K. Nikoskinen, "SAR variation study from 300 to 5000 MHz for 15 voxel models including different postures," *Phys. Med. Biol.*, vol. 55, no. 4, pp. 1157–1176, 2010.
[17] G. Vermeeren, W. Joseph, and L. Martens, "Statistical multi-path exposure method for assessing the whole-body SAR in a heterogeneous human body model in a realistic environment," *BioElectroMagnetics*, vol. 34, no. 3, pp. 240–251, 2013.
[18] D. Dunbar and G. Humphreys, "A spatial data structure for fast Poisson-disk sample generation," *ACM Trans. Graph.*, vol. 25, no. 3, pp. 503–508, Jul. 2006.
[19] M. Born and E. Wolf, *Principles of Optics: Electromagnetic Theory of Propagation, Interference and Diffraction of Light*. Amsterdam, The Netherlands: Elsevier, 2013.
[20] I. Laakso, "Assessment of the computational uncertainty of temperature rise and SAR in the eyes and brain under far-field exposure from 1 to 10 GHz," *Phys. Med. Biol.*, vol. 54, no. 11, pp. 3393–3404, 2009.
[21] M.-C. Gosselin *et al.*, "Development of a new generation of high-resolution anatomical models for medical device evaluation: The virtual population 3.0," *Phys. Med. Biol.*, vol. 59, no. 18, pp. 5287–5303, 2014.
[22] T. L. Marzetta, E. G. Larsson, H. Yang, and H. Q. Ngo, *Fundamentals of Massive MIMO*. Cambridge, U.K.: Cambridge Univ. Press, 2016.
[23] A. O. Martinez, E. De Carvalho, J. O. Nielsen, and L. Jing, "Frequency dependence of measured massive MIMO channel properties," in *Proc. IEEE 83rd Veh. Technol. Conf. (VTC Spring)*, May 2016, pp. 1–5.
[24] X. Gao, O. Edfors, F. Rusek, and F. Tufvesson, "Massive MIMO performance evaluation based on measured propagation data," *IEEE Trans. Wireless Commun.*, vol. 14, no. 7, pp. 3899–3911, Jul. 2015.
[25] S. R. Saunders, *Antennas and Propagation for Wireless Communication Systems*, 1st ed. New York, NY, USA: Wiley, 1999.
[26] A. Ahlbom *et al.*, "Guidelines for limiting exposure to time-varying electric, magnetic, and electromagnetic fields (up to 300 GHz)," *Health Phys*, vol. 74, no. 4, pp. 494–521, 1998.
[27] E. Tanghe *et al.*, "The industrial indoor channel: Large-scale and temporal fading at 900, 2400, and 5200 MHz," *IEEE Trans. Wireless Commun.*, vol. 7, no. 7, pp. 2740–2751, Jul. 2008.

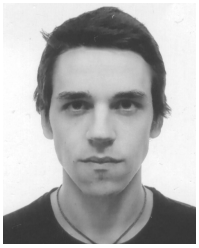

SERGEI SHIKHANTSOV received the B.Sc. and M.Sc. degrees in applied physics and mathematics from the Moscow Institute of Physics and Technology, Moscow, Russia, in 2014 and 2016, respectively. He is currently pursuing the Ph.D. degree in engineering physics with Ghent University, Ghent, Belgium. His research interests include computational electrodynamics, numerical assessment of human electromagnetic field exposure, and propagation modeling of the next-generation wireless networks.

ARNO THIELENS received the M.Sc. degree in engineering with specialization in applied physics from Ghent University, in 2010, and the Ph.D. degree in applied physics from the Waves Group, Information Technology Department, Ghent University, in 2015. From 2016 to 2017, he was a Postdoctoral Fellow with the Institute for Science and Innovation, Flanders, Belgium. In 2017, he joined the Berkeley Wireless Research Center, University of California, Berkeley, where he is involved in the development of the human intranet. Since 2015, he has been a Postdoctoral Researcher with Waves. His research focused on personal exposure assessment to radio-frequency electromagnetic fields and numerical dosimetry. He received the FWO [PEGASUS]^2 Marie Skłodowska-Curie Fellowship funded by the European Union's Horizon 2020 Research and Innovation Programme under Marie Skłodowska-Curie Grant Agreement No. 665501 with the research Foundation Flanders (FWO), in 2017. He also received the Honorary Fellowship by the Belgian American Education Foundation, in 2017, and the Joseph James Morrissey Memorial Award issued by the Bioelectromagnetics Society and the European Bio Electromagnetics Association, in 2013. He was a recipient of the 2015 International Union of Radio Science (Union Radio-Scientifique Internationale) Young Scientist Award.

GÜNTER VERMEEREN received the M.Sc. degree in industrial engineering from KAHO Sint-Lieven, Ghent, Belgium, in 1998, and the M.Sc. degree in electrical engineering and the Ph.D. degree in electro-technical engineering from Ghent University, Belgium, in 2001 and 2013, respectively. From 2001 to 2002, he was with the Research and Development Department, Telindus, Leuven, Belgium, a network integrator. Since 2002, he has been a Research Engineer with the WiCa Group of Prof. L. Martens. His researches focuss on the numerical modeling and measurements of electromagnetic radiation in the domain of radio-frequency dosimetry, electromagnetic exposure, on-body propagation, interference in communication networks, and medical imaging systems, such as, hybrid MRI systems.

EMMERIC TANGHE was born in Tielt, Belgium, in 1982. He received the M.Sc. and Ph.D. degrees in electrical engineering from Ghent University, Ghent, Belgium, in 2005 and 2011, respectively. From 2005 to 2011, he was a Research Assistant with the Department of Information Technology, Ghent University–imec. His scientific research focused on the modeling of indoor and outdoor propagation through field measurements. In 2015, he became a Part-Time Professor in medical applications of electromagnetic fields in and around the human body. Since 2011, he has been a Postdoctoral Researcher with Ghent University–imec, where he focuses on propagation modeling. From 2012 to 2018, he was a Postdoctoral Fellow of FWO-V (Research Foundation–Flanders).

PIET DEMEESTER (F'09) is currently a Professor with Ghent University–imec, Ghent, Belgium, where he is also the Department Director of the IDLab. He has co-authored over 1000 international publications. He holds an advanced ERC Grant. His research interests include distributed intelligence in the Internet of Things, machine learning and data mining, semantic intelligence, cloud and big data infrastructures, fixed networking, wireless networking, electromagnetics, and high-frequency design.

LUC MARTENS received the M.Sc. degree in electrical engineering from Ghent University, Ghent, Belgium, in 1986, and the Ph.D. degree, in 1990. From 1986 to 1990, he was a Research Assistant with the Department of Information Technology, Ghent University. During this period, his scientific research focused on the physical aspects of hyperthermic cancer therapy. His research dealt with electromagnetic and thermal modeling, and the development of measurement systems for that application. Since 1991, he has been managing the WAVES Research Group, INTEC. The WAVES Research Group is part of the imec Institute, since 2004. Since 1993, he has been a Professor with Ghent University. He has authored or co-authored more than 300 publications in the domain of electromagnetic channel predictions, dosimetry, exposure systems and health, and wireless communications. His research interests include modeling and measurement of electromagnetic channels, in electromagnetic exposure, e.g., around telecommunication networks and systems such as cellular base station antennas and in energy consumption of wireless networks.

GUY TORFS (M'13) received the Engineering degree in applied electronics and the Ph.D. degree in applied sciences and electronics from Ghent University, Ghent, Belgium, in 2007 and 2012, respectively. Since 2011, he has been with imec, associated with Ghent University, where he became an Assistant Professor, in 2015. His research interests include high-speed mixed-signal designs for wireless baseband and fiber-optic and backplane communication systems, digital signal processing and calibration, analog equalization circuits, and clock and data recovery systems. He was a recipient of the Greentouch 1000x Award, as part of the Bi-PON and Cascaded Bi-PON Team, in 2014. He was a co-recipient of the 2015 DesignCon Best Paper Award in the High-Speed Signal Design Category. He serves as an Associate Editor for IEEE TCAS-II and IEICE Elex.

WOUT JOSEPH was born in Ostend, Belgium, in 1977. He received the M.Sc. and Ph.D. degrees in electrical engineering from Ghent University, Ghent, Belgium, in 2000 and 2005, respectively. From 2000 to 2005, he was a Research Assistant with the Department of Information Technology, Ghent University. During this period, his scientific research focused on electromagnetic exposure assessment. Since 2005, he has been a Postdoctoral Researcher with INTEC, UGent–imec. Since 2009, he has been a Professor in the domain of experimental characterization of wireless communication systems. His research interests include measuring and modeling electromagnetic fields around base stations for mobile communications, health effects of exposure to electromagnetic radiation, electromagnetic exposure assessment, propagation for wireless communication systems, and antennas and calibration. He is specialized in wireless performance analysis and quality of experience. From 2007 to 2013, he was a Postdoctoral Fellow of the FWO-V (Research Foundation-Flanders).